SUPPLEMENTARY INFORMATION FOR

Synergistic effects of charge transfer, energy transfer and cavity interference on exciton emission in WS_2/hBN/WS_2 heterostructures

Zheyuan Xu[a,b], Jinyue Fu[a,b], Wenlong Jiang[a,b], Ying Chen[c], Boyi Xu[a,b], Sheng-Yi Xie[a], Ying Jiang*[a,b], and Anlian Pan*[b,d]

[a] *School of Physics and Electronics, and College of Materials Science and Engineering, Hunan University, Changsha, Hunan 410082, China*

[b] *Key Laboratory for Micro-Nano Physics and Technology of Hunan Province, Hunan Institute of Optoelectronic Integration, Hunan University, Changsha, Hunan 410082, China*

[c] *State Key Laboratory of Pulsed Power Laser Technology, Key Laboratory of Electronic Restriction of Anhui Province, National University of Defense Technology, Advanced Laser Technology Laboratory of Anhui Province, Hefei 230037, China*

[d] *School of Physics and Electronics, Hunan Normal University, Changsha, Hunan 410081, China*

*Address correspondence to Ying Jiang, jying@hnu.edu.cn; Anlian Pan, anlian.pan@hnu.edu.cn

Section 1. Variation in spectrum of ME-WS_2/hBN/CVD-WS_2 on SiO_2/Si substrate as a function of hBN thickness

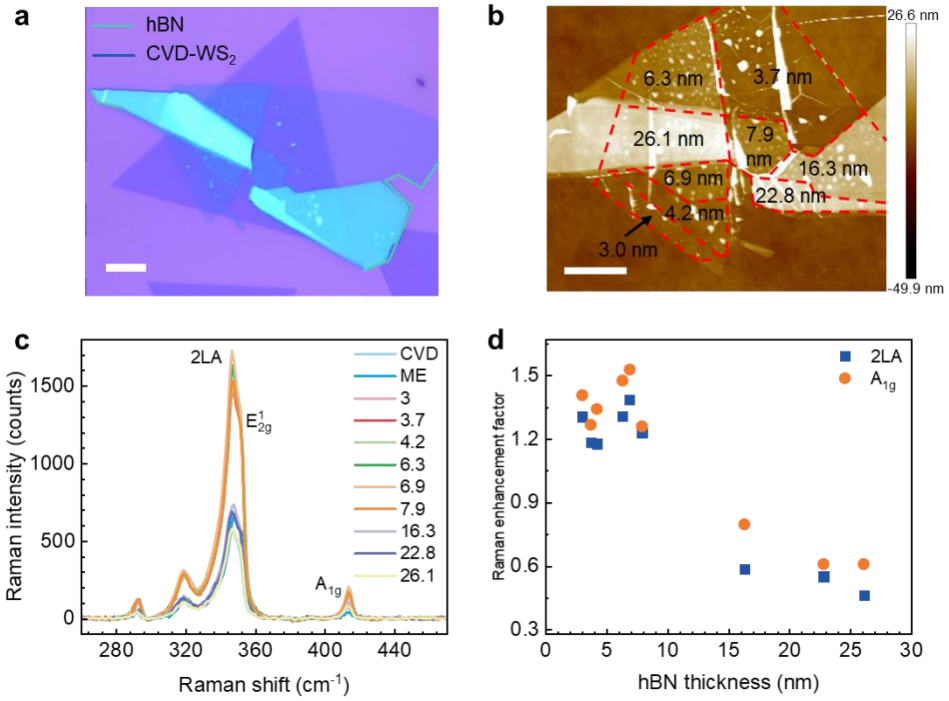

Figure S1 (a) Optical image of the hBN/CVD-WS_2 sample before transferring the top ME-WS_2 layer. (b) Atomic force microscope (AFM) height mapping of the sample in (a). Scale bars in (a) and (b) are 10 μm. (c) Measured Raman spectra of the sample on various thicknesses of hBN. (d) Raman enhancement factors of the sample as a function of hBN thickness. The Raman enhancement factor was obtained by dividing the Raman peak intensity of HS1 by the sum of the Raman peak intensities of ME-WS_2 and CVD-WS_2.

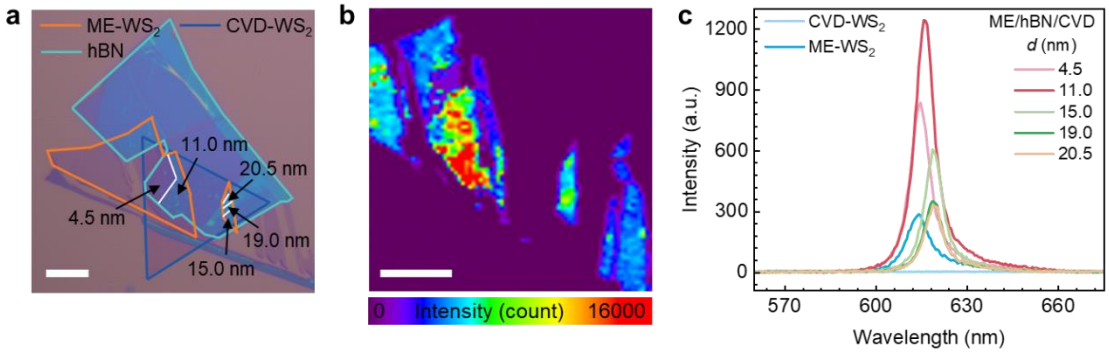

Figure S2 (a) Optical image of the ME-WS_2/hBN/CVD-WS_2 sample on SiO_2/Si substrate. (b) PL intensity mapping of the sample in (a). Scale bars: (a) 20 are (b) 10

μm. (c) Measured PL spectra of the sample in (a) on various thicknesses of hBN.

Section 2. hBN thickness-dependent PL measurements

To clearly illustrate the influence of hBN thickness on the exciton peak position, we plotted the PL peak position as a function of hBN thickness for the ME-WS_2/hBN/CVD-WS_2 heterostructure, as shown in Fig. S3. We observe a significant change in the PL peak position with increasing hBN thickness of the heterostructure, characterized by a continuous red-shift (red dashed line) that saturates at approximately 619.2 nm around a hBN-thickness of 10 nm. Our results are in excellent agreement with previously reported trends,[1-3] indicating the dominant role of dielectric screening. However, deviations from this trend were observed in the PL peak positions of some samples, which can be attributed to the introduction of impurities, wrinkles, and cracks during the sample transfer process. These imperfections can alter the dielectric environment and stress, thereby affecting the exciton energy.

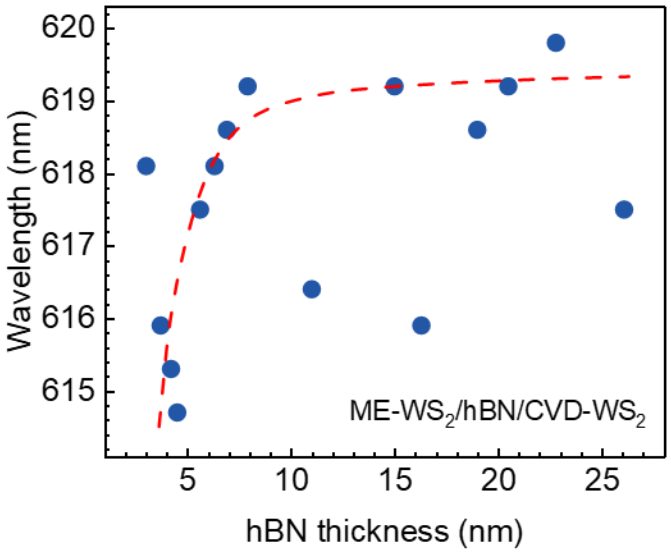

Figure S3 hBN thickness-dependent PL peak position of ME-WS_2/hBN/CVD-WS_2.

To mitigate the impact of spatial inhomogeneity on the exciton peak position, we extracted five PL spectra from spatially homogeneous regions within the PL mapping data for each hBN thickness. For some samples, such as the hBN-15.0 nm sample, only a single PL spectrum was obtained due to morphological constraints. From these spectra, we extracted the PL peak positions and plotted them as a function of hBN thickness,

incorporating error bars to represent the variability in peak position (Fig. S4a). This analysis reveals a more pronounced thickness dependence: the PL peak position exhibits a gradual redshift from ~614 nm with increasing hBN thickness, saturating at ~619 nm around 10 nm. Furthermore, we extracted the PL peak intensity as a function of hBN thickness (Fig. S4b), revealing a trend consistent with that observed in Fig. 1e, further validating our experimental observations.

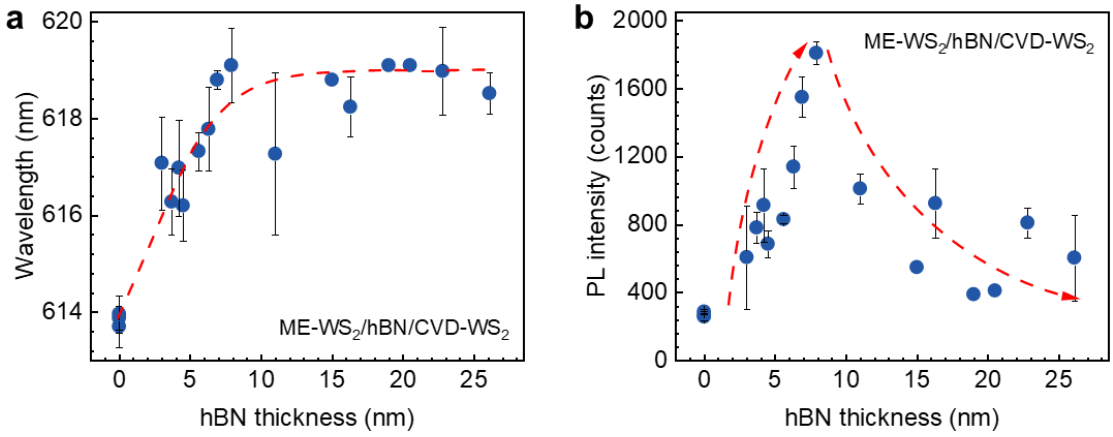

Figure S4 hBN thickness-dependent PL peak position (a) and PL intensity (b) of ME-WS_2/hBN/CVD-WS_2.

Section 3. Effect of strain on the PL peak position of CVD-WS_2

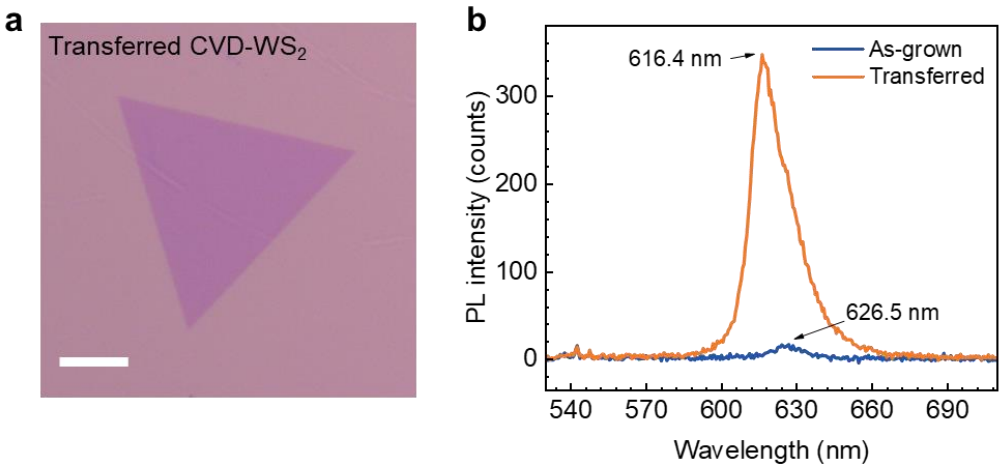

Figure S5 (a) Optical image of transferred CVD-WS_2 to SiO_2/Si substrate. It was prepared by gluing the as-grown CVD-WS_2 from the SiO_2/Si substrate and then transferring it to the same substrate. Scale bar: 10 μm. (b) PL spectra of as-grown and transferred CVD-WS_2.

Section 4. Variation in TRPL of ME-WS_2/hBN/CVD-WS_2 as a function of hBN thickness

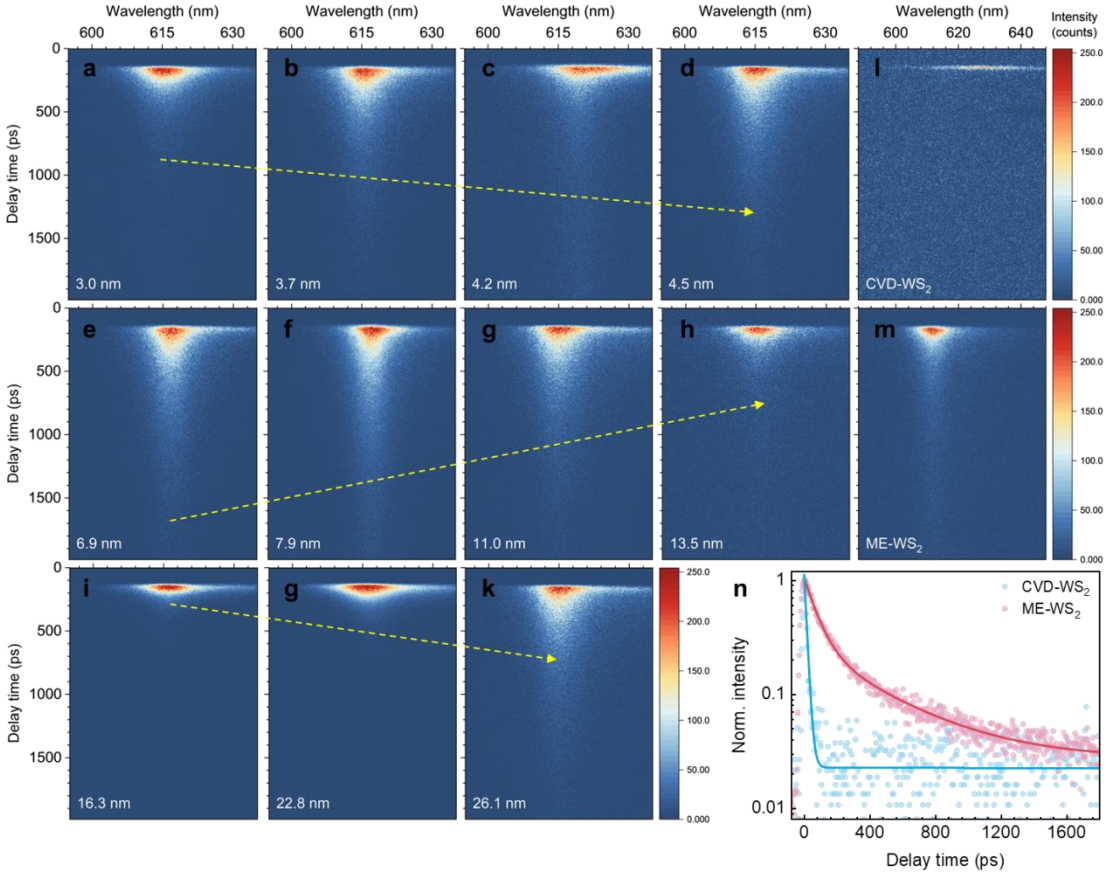

Figure S6 (a-k) Streak camera images collected from the ME-WS_2/hBN/CVD-WS_2 HS1 with different thicknesses of the hBN interlayer. A remarkable three-stage variation can be found, where the lifetime first prolongs and then shortens followed by lengthens as the hBN thickness increases. (l, m) Streak camera images collected from CVD-WS_2 monolayer (l) and ME-WS_2 monolayer (m). (n) Extracted time-resolved PL from CVD-WS_2 monolayer (l) and ME-WS_2 monolayer (m).

Table S1 TRPL fitting parameters of CVD-WS_2 monolayer, ME-WS_2 monolayer and ME-WS_2/hBN/CVD-WS_2 HS1 with different hBN thikness.

Sample	τ_1 (ps)	A_1 (%)	τ_2 (ps)	A_2 (%)	τ_{ave} (ps)
CVD			14.6 ± 0.3		14.6
ME	76.2 ± 1.1	75.5	430.3 ± 22.9	24.5	163.0
3.0	101.5 ± 1.8	85.2	371.1 ± 30.1	14.8	141.4

3.7	121.5 ± 5.6	56.8	401.8 ± 21.3	43.2	242.6
4.2	104.2 ± 5.0	42.1	416.1 ± 12.0	57.9	284.8
4.5	115.7 ± 5.9	54.1	479.7 ± 26.9	45.9	282.8
6.9	123.4 ± 5.8	49.0	488.4 ± 21.3	51.0	309.6
7.9	80.6 ± 2.6	44.0	480.1 ± 9.2	56.0	304.3
11.0	79.7 ± 1.9	44.8	400.2 ± 15.8	55.2	256.6
13.5	72.0 ± 1.0	79.5	381.3 ± 25.3	20.5	135.4
16.3	50.0 ± 0.6	96.6	355.1± 67.7	3.4	60.4
22.8	48.1 ± 0.3	96.8	357.5 ± 34.5	3.2	58.0
26.1	64.6 ± 0.6	93.7	376.7 ± 35.9	6.3	84.3

Section 5. Effects of CT and ET on exciton dynamics

In order to evaluate the effect of CT and ET processes on the carrier dynamics in CVD-WS_2 and ME-WS_2 layer, we introduce rate equations for exciton dynamics.[4] In the individual CVD-WS_2 and ME-WS_2 monolayer, excitons recombine in radiative and non-radiative manner with the rate of k_r and k_{nr} (Figs. S7a, b). Thus, the rate equations can be expressed as

$$\frac{dN_{CVD}}{dt} = -\left(k_{r,CVD} + k_{nr,CVD}\right) N_{CVD}, \quad (1)$$

$$\frac{dN_{ME}}{dt} = -\left(k_{r,ME} + k_{nr,ME}\right) N_{ME}, \quad (2)$$

where N is exciton density in individual monolayer. We can obtain the decay rate of the exciton as $k_{CVD}^{m} = k_{r,CVD} + k_{nr,CVD}$ in CVD-WS_2 monolayer and $k_{ME}^{m} = k_{r,ME} + k_{nr,ME}$ in ME-WS_2 monolayer.

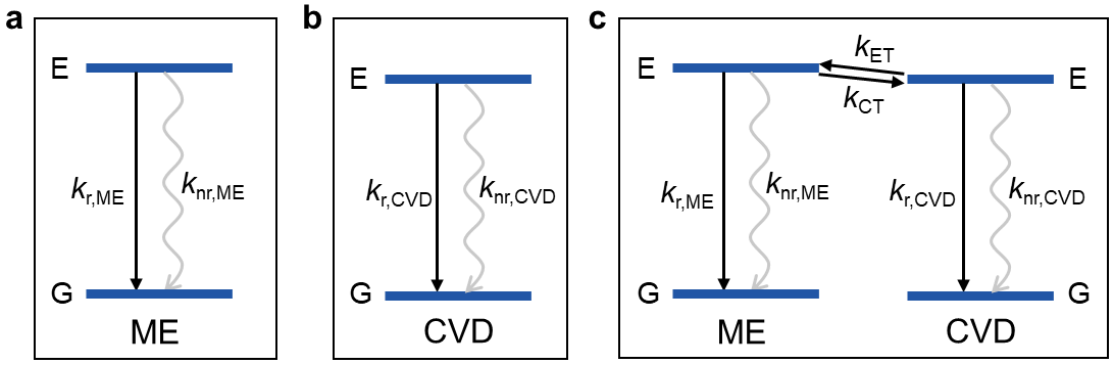

Figure S7 (a-c) Energy diagrams representing exciton relaxation channels in ME-WS_2/hBN/ME-WS_2 heterostructure. In ME-WS_2 (a) and CVD-WS_2 (b) monolayers, excitons decay through radiative and non-radiative channels. In ME-WS_2/hBN/CVD-WS_2 HS1 (c), the presence of ET from CVD-WS_2 to ME-WS_2 and CT channels from ME-WS_2 to CVD-WS_2 modifies the exciton dynamics in both layers.

In the ME-WS_2/hBN/CVD-WS_2 HS1, CT from ME-WS_2 to CVD-WS_2 and ET from CVD-WS_2 to ME-WS_2 with the rate of k_{CT} and k_{ET} will occur (Fig. S7c), according to the analysis in the main text. Therefore, the rate equations for each layer in the HS1 change to

$$\frac{dN_{CVD}}{dt} = -\left(k_{r,CVD} + k_{nr,CVD} + k_{ET}\right) N_{CVD} + k_{CT} N_{ME}, \quad (3)$$

$$\frac{dN_{ME}}{dt} = -\left(k_{r,ME} + k_{nr,ME} + k_{CT}\right) N_{ME} + k_{ET} N_{CVD}, \quad (4)$$

For simplicity, we assume that k_r and k_{nr} in two layers are unaffected when changing the hBN thickness. For CVD-WS_2 layer in HS1, following the excitation to form an exciton, an additional exciton formation channel with a rate of k_{CT} becomes operative, which is reflected in the rising edge of the TRPL. And, the decay rate of excitons $k_{CVD}^{HS} = k_{r,CVD} + k_{nr,CVD} + k_{ET} = k_{CVD}^{m} + k_{ET}$ is accelerated relative to the CVD-WS_2 monolayer due to the presence of an additional decay channel of ET. Consequently, the ET rate can be calculated by the change in lifetime of the energy donor (CVD-WS_2 in our study) in the HS1 relative to the monolayer, a method that has been widely adopted in various systems.[5, 6]

For ME-WS_2 layer in HS1, the secondary rise time at rate k_{ET} and the exciton decay rate $k_{ME}^{HS} = k_{r,ME} + k_{nr,ME} + k_{CT} = k_{ME}^{m} + k_{CT}$ can be obtained. Consequently, when the CT process is effective or when the hBN is relatively thin, the exciton lifetime $\tau_{ME} = 1/k_{ME}^{HS}$ in ME-WS_2 layer is significantly reduced compared to the monolayer. As the thickness of hBN increases, the k_{CT} is gradually invalidated, and the exciton recombination time is prolonged. Until the hBN thickness reaches a sufficient magnitude, the CT is completely neglected, and the carrier lifetime is stabilized at a value equivalent to that of the monolayer. In any case, the ET process has no effect on exciton decay.

Section 6. Variation in optical properties of ME-WS_2/hBN on SiO_2/Si substrate as a function of hBN thickness

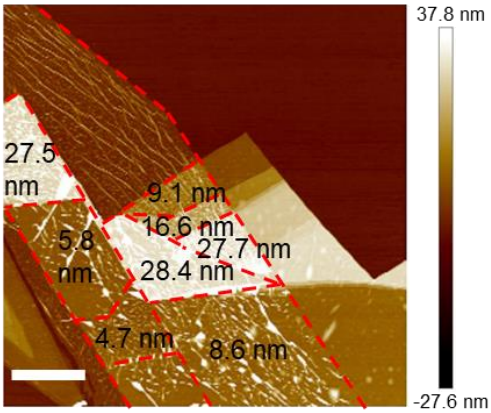

Figure S8 AFM height mapping of the ME-WS_2/hBN HS2. Scale bar: 10 μm.

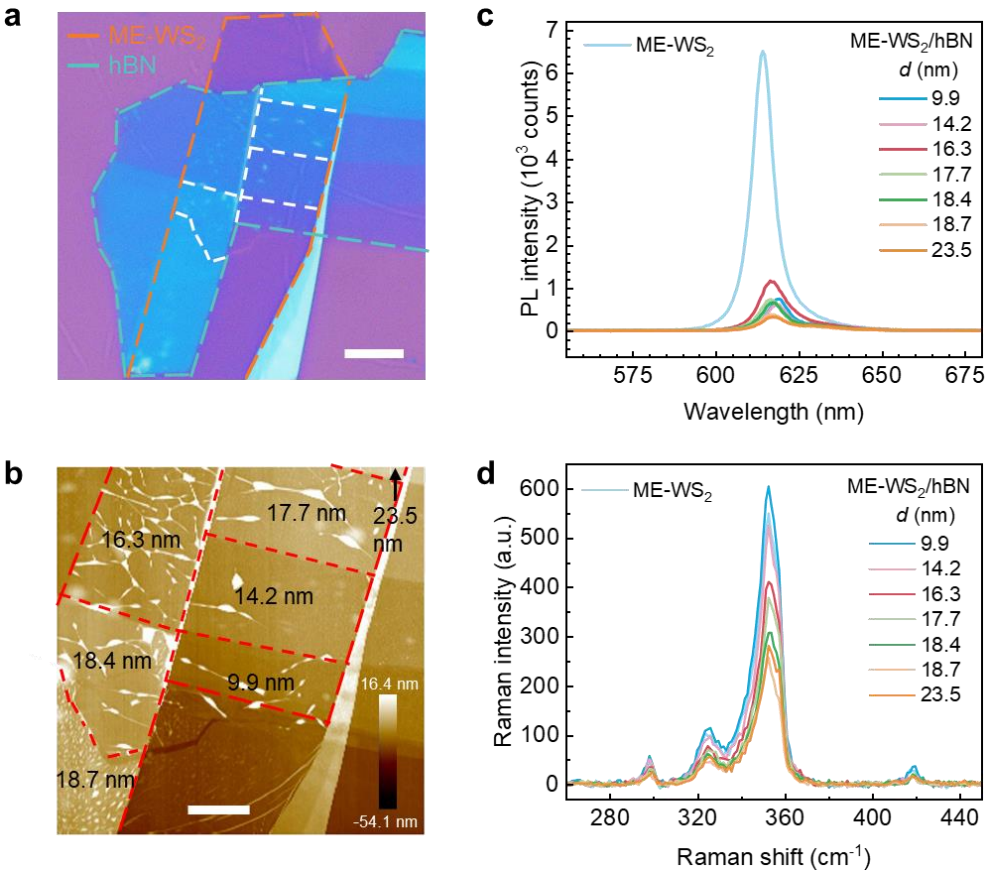

Figure S9 (a, b) Optical image (a) and AFM height mapping (b) of the ME-WS_2/hBN sample on SiO_2/Si substrates. Scale bar: (a) 10 and (b) 5 μm. (c, d) Measured PL (c) and Raman (d) spectra of ME-WS_2/hBN HS2 on various thicknesses of hBN.

Section 6. Enhancement factors of ME-WS_2/hBN samples as a function of hBN thickness

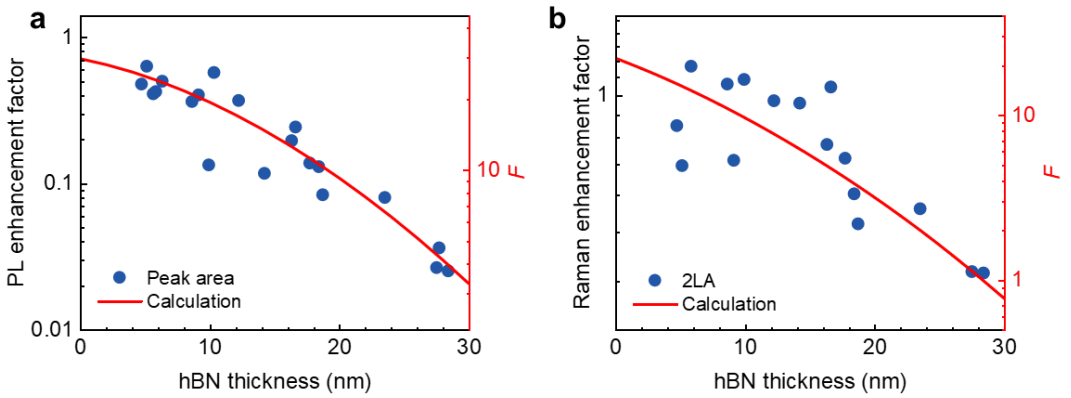

Figure S10 (a) PL enhancement factors derived from peak area of ME-WS_2/hBN samples as a function of hBN thickness. (b) Raman (A_{1g} mode) enhancement factors of ME-WS_2/hBN as a function of hBN thickness. The solid red line is the intensity factor obtained from the optical interference model.

Section 8. Optical interference effect on the PL and Raman intensity

When light propagates within a medium, interference effects emerge due to the reflection and refraction of light at various interfaces, which can influence the spatial distribution of the optical field. Considering that the intensity of the detected signal is influenced by both the excitation light field and the emitted light field, suggesting a potential for significant modulation through optical interference effects. This phenomenon has been thoroughly investigated by modulating the PL of the TMD by varying the thickness of the dielectric layer at the base of the TMD material, thereby achieving up to two orders of magnitude of intensity modulation.[7, 8] Fig. S9 illustrates the optical interference schematic for a five-layer system, wherein layers 0 to 4 are composed of air, WS_2 monolayer, hBN, SiO_2, and Si, respectively. Multiple reflections of incident light (left) and emitted light (right, PL or Raman signals) are plotted for this system. The red point in the layer 1 (WS_2 monolayer) is a point at a distance of x depth from the interface between layer 0 (air) and layer 1, where absorption and emission occur. d_i is the thickness of layer i. The thickness of WS_2 monolayer (d_1) is taken to be 0.7 nm.

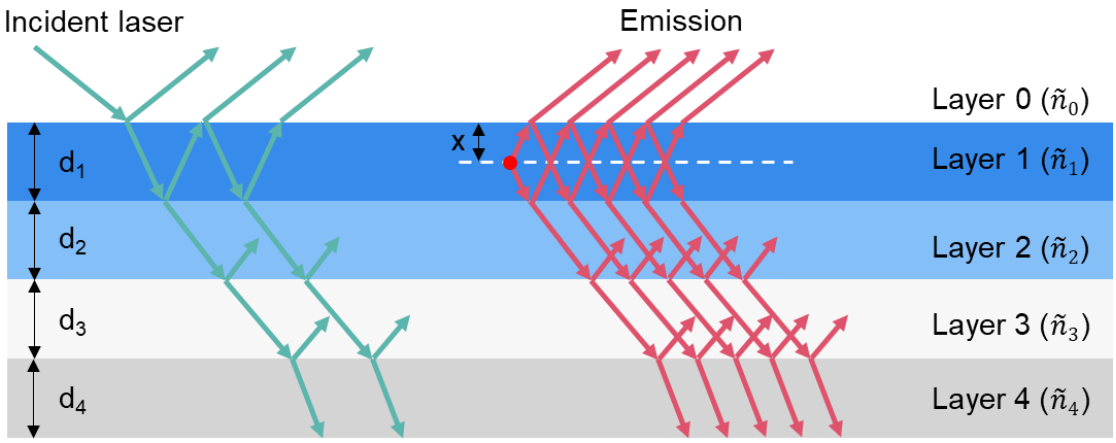

Figure S11 Schematic diagram of the optical interference effect in a five-layered system.

The net absorption of incident light by the WS_2 monolayer and the net emission from the WS_2 monolayer in the four-layered system can be expressed as[7, 9, 10]

$$E_{in} = t_1 \frac{[1 + r_2 r_3 e^{-2i\beta_2}]e^{-i\beta_x} + [r_2 + r_3 e^{-2i\beta_2}]e^{-i(2\beta_1 - \beta_x)}}{1 + r_2 r_3 e^{-2i\beta_2} + (r_2 + r_3 e^{-2i\beta_2}) r_1 e^{-2i\beta_1}}, \quad (5)$$

$$E_{emit} = t_1' \frac{[1 + r_2' r_3' e^{-2i\beta_2'}]e^{-i\beta_x'} + [r_2' + r_3' e^{-2i\beta_2'}]e^{-i(2\beta_1' - \beta_x')}}{1 + r_2' r_3' e^{-2i\beta_2'} + (r_2' + r_3' e^{-2i\beta_2'}) r_1' e^{-2i\beta_1'}}, \quad (6)$$

where $t_1 = \frac{2\tilde{n}_0}{\tilde{n}_0 + \tilde{n}_1}$, $r_i = \frac{\tilde{n}_{i-1} - \tilde{n}_1}{\tilde{n}_{i-1} + \tilde{n}_1}$, $\beta_i = \frac{2\pi d_i \tilde{n}_i}{\lambda}$, $\beta_x = \frac{2\pi x \tilde{n}_1}{\lambda}$ and $\tilde{n}_i$ are corresponding to the wavelength of incident laser λ (532 nm). t_1 is the Fresnel transmission from layer 1 (WS_2) to layer 0 (air) at normal incidence. r_i is the Fresnel reflection coefficient at the interface between the different layers at normal incidence. $\tilde{n}_i$ is the refractive index of layer i. $t_1' = \frac{2\tilde{n}_1'}{\tilde{n}_0' + \tilde{n}_1'}$, r_i' , β_i' , β_x' and $\tilde{n}_i$ are corresponding to the wavelength of emitting light λ', which was fixed at 615 nm for PL and 532 nm for Raman. For five-layered system (air/WS_2/hBN/SiO_2/Si), r_3 in equation (5) and r_3' in equation (6) should be replaced by $\frac{r_3 + r_4 e^{-2i\beta_3}}{1 + r_3 r_4 e^{-2i\beta_3}}$ and $\frac{r_3' + r_4' e^{-2i\beta_3'}}{1 + r_3' r_4' e^{-2i\beta_3'}}$. Further, for six-layered system (air/WS_2/hBN/WS_2/SiO_2/Si in our study), r_4 in five-layered system should be replaced by $\frac{r_4 + r_5 e^{-2i\beta_4}}{1 + r_4 r_5 e^{-2i\beta_4}}$, r_4' makes the similar substitution.

Then, the total intensity factor *F* is given by

$$F = \int_0^{d_1} \left| E_{in} E_{emit} \right|^2 dx. \quad (7)$$

The complex refractive indices of the materials that were used for the calculations are given in Table S2. The thickness of SiO_2 taken to be 300 nm. The calculated *F* of PL and Raman for five-layered system (air/WS_2/hBN/SiO_2/Si) and six-layered system (air/WS_2/hBN/WS_2/SiO_2/Si) are shown in Figs. S12 and S13.

The spontaneous radiation of carriers arises from the interaction of the quantum jump dipole moment with the cavity mode electric field, and the rate of radiation is

proportional to the square of the electric field intensity. Therefore, we calculate the electric field intensity factor F_{in},

$$F_{in} = \int_0^{d_1} |E_{in}|^2 \, dx. \tag{8}$$

The wavelength of the incident laser is 400 nm. The calculated F_{in} for five-layered system (air/WS_2/hBN/SiO_2/Si) and six-layered system (air/WS_2/hBN/WS_2/SiO_2/Si) are shown in Figs. S12c and S13b.

Table S2 Details of refractive indices of the materials used for the calculations.

Materials	Wavelength (nm)	Indices (n-ik)		References
		n	k	
WS_2	400 (excitation)	3.79	2.75	[11]
	532 (excitation/ emission)	4.9	0.9	
	615 (emission)	4.9	1.8	
hBN	400	2.15	0	[12]
	532	2.13	0	
	615	2.13	0	
SiO_2	400	1.47	0	[13]
	532	1.46	0	
	615	1.46	0	
Si	400	5.57	0.39	[14]
	532	4.15	0.05	
	615	3.9	0.02	

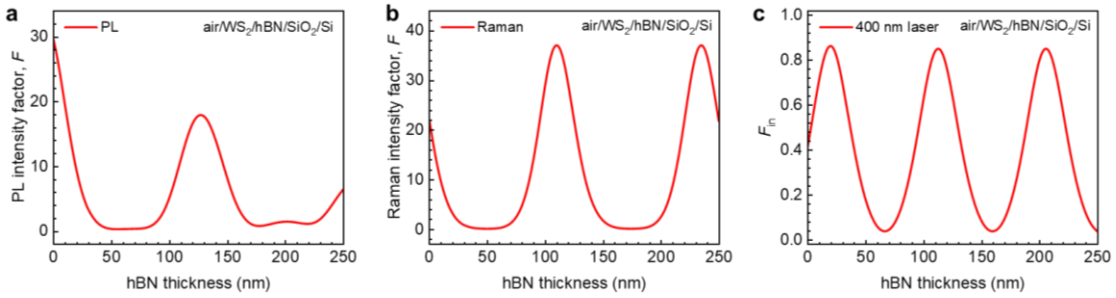

Figure S12 (a, b) Calculated PL and Raman intensity factors of air/WS_2/hBN/SiO_2/Si as a function of the thickness of the thickness layer. (c) Calculated electric field intensity factor (F_{in}) of air/WS_2/hBN/SiO_2/Si as a function of the hBN thickness.

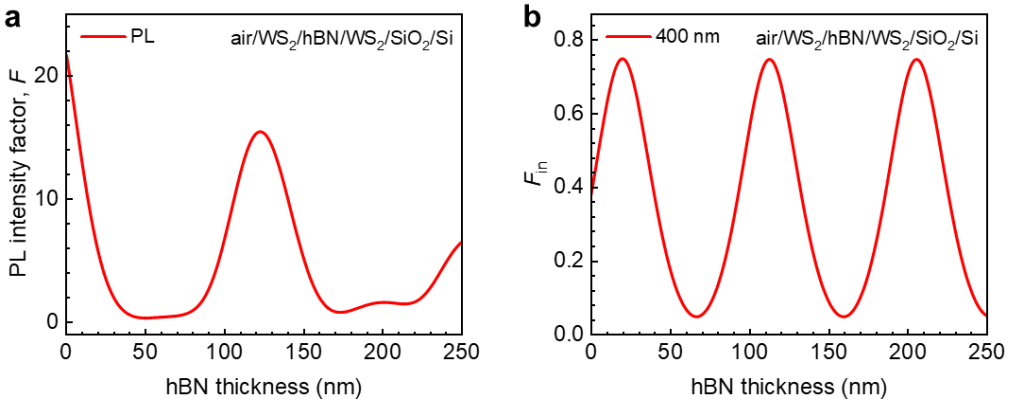

Figure S13 (a, b) Calculated PL intensity factors (F, a) and electric field intensity factor (F_{in}, b) of air/WS_2/hBN/WS_2/SiO_2/Si as a function of the hBN thickness.

Section 9. Variation in TRPL of WS_2/hBN on SiO_2/Si substrate as a function of hBN thickness

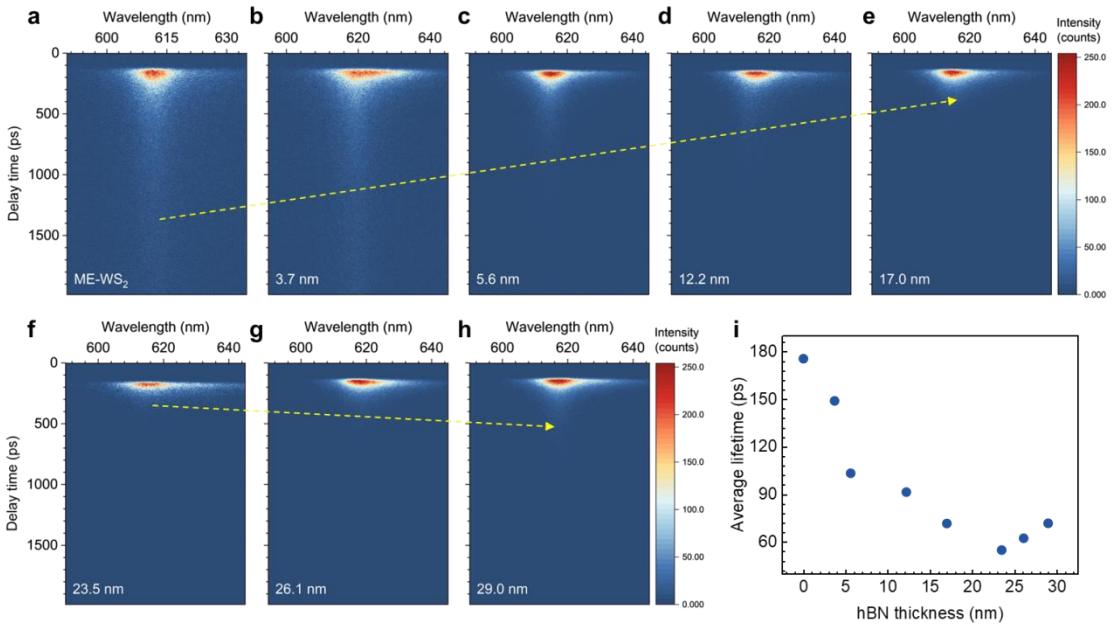

Figure S14 (a-h) Streak camera images collected from the ME-WS_2 monolayer (a) and ME-WS_2/hBN HS2 (b-h) with different thicknesses of the hBN interlayer. Obviously, the carrier decay accelerates and then decelerates as the hBN thickness increases. (i) The average lifespan obtained from the fit.

Table S3 TRPL fitting parameters of ME-WS_2 monolayer and ME-WS_2/hBN HS2 with different hBN thikness.

Sample	τ_1 (ps)	A_1 (%)	τ_2 (ps)	A_2 (%)	τ_{ave} (ps)
ME	81.9 ± 1.3	72.7	425.3 ± 19.6	27.3	175.6
3.7	77.0 ± 2.2	75.0	365.1 ± 25.3	25.0	149.0
5.6	68.5 ± 1.6	86.1	319.2 ± 22.9	13.9	103.3
12.2	59.4 ± 1.5	86.8	301.9 ± 29.6	13.2	91.4
17.0	58.8 ± 1.4	93.1	243.8 ± 20.9	6.9	71.6
23.5	50.5 ± 0.6	97.8	245.5 ± 25.1	2.2	54.8
26.1	52.1 ± 0.5	95.0	256.2 ± 24.3	5.0	62.3
29.0	68.5 ± 1.6	93.4	277.6 ± 19.3	6.6	71.7

Section 10. Effects of CT, ET and cavity interference on exciton dynamics

The rate of exciton recombination is regulated by the radiative recombination (k_r) being modulated by the cavity interference effect, the CT (k_{CT}) and other non-radiative recombination channels except CT (k_{nr}). The ET process does not modify the decay dynamics of the acceptor ME-WS_2, and thus it is not necessary to consider it in this context.

The radiative recombination rate of the excitons $k_r(d)$ is controlled by the Purcell effect, which can be well described by the electric field intensity factor $F_{in}(d)$ (Figs. 4c, d in the main text). Thus, the radiative recombination rate can be given by

$$k_r(d) = aF_{in}(d)k_0, \tag{9}$$

where a is a dimensionless coefficient, k_0 is the exciton recombination rate in the suspended WS_2 monolayer.

CT involves the exchange of electrons between donor and acceptor. It is classified as a non-radiative process, and its rate of occurrence is directly exponentially with the distance between the donor and acceptor. The CT rate can be expressed as[15]

$$k_{CT}(d) = be^{-\frac{2d}{L}}, \tag{10}$$

where b is a dimensionless coefficient, d is the distance between the donor and acceptor, and L is the sum of the exciton Bohr radii of the donor and acceptor. Here we simply consider the exciton Bohr radius of the two WS_2 layers to be the same, i.e., $L = 2r_0$, and $r_0 = 1.1$ nm is the exciton Bohr radius of the WS_2 monolayer which is referred to the previous reported value.[16-18]

It can be reasonably assumed that non-radiative recombination processes other than charge transfer do not vary with hBN thickness, i.e.,

$$k_{nr}(d) = k_{nr}, \tag{11}$$

Therefore, we can obtain the total decay rate of excitons in ME-WS_2 as

$$k(d) = k_r + k_{CT} + k_{nr} = aF_{in}(d)k_0 + be^{-\frac{d}{r_0}} + k_{nr}. \quad (12)$$

By adjusting the parameters ak_0 and b, it is possible to modulate the relative strengths of the CT and cavity interference effects. Consequently, this adjustment allows for the modulation of the exciton decay rate as a function of hBN thickness. It is demonstrated that this line shape acquired by equation (12), corresponds precisely to the experimental results (Fig. 5 in the main text).

References

1. A. Raja, A. Chaves, J. Yu, G. Arefe, H. M. Hill, A. F. Rigosi, T. C. Berkelbach, P. Nagler, C. Schüller, T. Korn, C. Nuckolls, J. Hone, L. E. Brus, T. F. Heinz, D. R. Reichman and A. Chernikov, *Nat. Commun.*, 2017, **8**, 15251.
2. I. C. Gerber and X. Marie, *Phys. Rev. B*, 2018, **98**, 245126.
3. A. O. Slobodeniuk and M. R. Molas, *Phys. Rev. B*, 2023, **108**, 035427.
4. D. Kozawa, A. Carvalho, I. Verzhbitskiy, F. Giustiniano, Y. Miyauchi, S. Mouri, A. H. Castro Neto, K. Matsuda and G. Eda, *Nano Lett.*, 2016, **16**, 4087-4093.
5. N. Taghipour, P. L. Hernandez Martinez, A. Ozden, M. Olutas, D. Dede, K. Gungor, O. Erdem, N. K. Perkgoz and H. V. Demir, *ACS Nano*, 2018, **12**, 8547-8554.
6. A. Karmakar, A. Al-Mahboob, C. E. Petoukhoff, O. Kravchyna, N. S. Chan, T. Taniguchi, K. Watanabe and K. M. Dani, *ACS Nano*, 2022, **16**, 3861-3869.
7. Y. Lee, J. D. a. S. Forte, A. Chaves, A. Kumar, T. T. Tran, Y. Kim, S. Roy, T. Taniguchi, K. Watanabe, A. Chernikov, J. I. Jang, T. Low and J. Kim, *Nat. Commun.*, 2021, **12**, 7095.
8. X. Bao, J. Shi, X. Han, K. Wu, X. Zeng, Y. Xia, J. Zhao, Z. Zhang, W. Du, S. Yue, X. Wu, B. Wu, Y. Huang, W. Zhang and X. Liu, *Nano Lett.*, 2025, **25**, 2639-2646.
9. D. Yoon, H. Moon, Y.-W. Son, J. S. Choi, B. H. Park, Y. H. Cha, Y. D. Kim and H. Cheong, *Phys. Rev. B*, 2009, **80**, 125422.
10. H. Zhang, Y. Wan, Y. Ma, W. Wang, Y. Wang and L. Dai, *Appl. Phys. Lett.*, 2015, **107**, 101904.
11. G.-H. Jung, S. Yoo and Q. H. Park, *Nanophotonics*, 2019, **8**, 263-270.
12. P. G. Zotev, Y. Wang, D. Andres-Penares, T. Severs-Millard, S. Randerson, X. Hu, L. Sortino, C. Louca, M. Brotons-Gisbert, T. Huq, S. Vezzoli, R. Sapienza, T. F. Krauss, B. D. Gerardot and A. I. Tartakovskii, *Laser Photonics Rev.*, 2023, **17**, 2200957.
13. C. Z. Tan, *J. Non-Cryst. Solids*, 1998, **223**, 158–163

14. D. E. Aspnes and A. A. Studna, *Phys. Rev. B*, 1983, **27**, 985-1009.
15. C. Bradac, Z.-Q. Xu and I. Aharonovich, *Nano Lett.*, 2021, **21**, 1193-1204.
16. T. Cheiwchanchamnangij and W. R. L. Lambrecht, *Phys. Rev. B*, 2012, **85**, 205302.
17. T. C. Berkelbach, M. S. Hybertsen and D. R. Reichman, *Phys. Rev. B*, 2013, **88**, 045318.
18. D. Y. Qiu, F. H. da Jornada and S. G. Louie, *Phys. Rev. Lett.*, 2013, **111**, 216805.